


 Cite this: *New J. Chem.*, 2018, 42, 18678

Porosity- and content-controlled metal/metal oxide/metal carbide@carbon (M/MO/MC@C) composites derived from MOFs: mechanism study and application for lithium-ion batteries†

 Min Seok Kang,^a Dae-Hyuk Lee,^b Kyung-Jae Lee,^b Hee Soo Kim,^a Jihoon Ahn,^c Yung-Eun Sung ^{*b} and Won Cheol Yoo ^{*ad}

Implementation of metal–organic frameworks (MOFs) as a precursor and/or template to synthesize metal/metal oxide/metal carbide nanoparticles within a carbon framework (M/MO/MC@C) via thermolysis has attracted considerable interest for electrochemical applications. In particular, the tunability of the weight content and crystallinity of M/MO/MC nanoparticles and porosity control of the morphology-preserved carbon matrix are highly desirable factors for governing the electrochemical performance of M/MO/MC@C composites. Herein, we report a facile synthesis method for adjusting the porosity, content, and crystallinity of M/MO/MC@C composites that are pseudomorphically converted from MOFs (M-HKUST-1, M: Cu and Zn; M-MOF-74, M: Co, Fe, Mg; and ZIF-8). Vapor phase polymerization (VPP), which is a site-specific gas-phase polymerization occurring at open metal sites of MOFs, was first employed to prepare morphology- and crystallinity-preserved polymer@MOF composites, which were then subjected to thermolysis to obtain M/MO@C composites. The polymer content used for VPP was directly related to the M/MO/MC nanoparticle weight content as well as the porosity of the carbon framework. In addition, crucial factors governing the crystallinity of final M/MO/MC nanoparticles were clearly classified in terms of the standard reduction potential of metal nodes and thermodynamic calculation for carbothermic reduction and carbide formation. To identify the advantages of morphology-preserved and content- and porosity-optimized MO@C composites for electrochemical applications, a series of CuO@C samples and CuO obtained from the direct oxidation of MOFs were tested as anode materials for lithium-ion batteries (LIBs). The optimized CuO@C sample exhibited superior electrochemical performance, for instance outstanding long-term stability with a remarkable specific capacity of 410 mA h g^{−1} after 1000 cycles at a rate of 1000 mA g^{−1}.

 Received 27th September 2018,
Accepted 18th October 2018

DOI: 10.1039/c8nj04919j

rsc.li/njc

Introduction

Recently, metal–organic frameworks (MOFs), which are porous crystalline materials composed of metal nodes and organic linkers, have been widely utilized as precursors for constructing hybrid metal materials (e.g., metal/metal oxide) and carbonaceous materials.^{1,2} The regular arrangement of metal nodes in MOFs can easily be transformed to metal/metal oxide nanoparticles

(M/MO) through thermolysis and organic struts can be turned into a carbonaceous framework simultaneously, eventually producing metal/metal oxide nanoparticles within a carbon framework (M/MO@C). Nano-sized metal species spatially arranged within a carbon matrix (CM) have attracted considerable interest for electrochemical applications such as supercapacitors,^{3–6} lithium-ion batteries (LIBs),^{6–10} and fuel cells.^{11–13}

To achieve high-performance MOF-derived M/MO@C composites for electrochemical applications, the ability to tune the content, crystallinity, and size of M/MO as well as the porosity of the CM while preserving the morphology of the parent MOFs used is highly necessary. For example, MOFs undergo thermolysis under oxidation conditions. HKUST-1 ([Cu₃(btc)₂]) was oxidized under air at 500 °C to produce CuO nanoparticles¹⁴ and at 350 °C to produce CuO/Cu₂O mixed nanoparticles,¹⁵ both of which were utilized as anode materials for LIBs. Lou's group reported that Prussian blue microcubes were oxidized using a three-step process at temperatures of 350,

^a Department of Applied Chemistry, Hanyang University, Ansan 15588, Republic of Korea. E-mail: wcyoo@hanyang.ac.kr

^b Center for Nanoparticle Research Institute for Basic Science (IBS), Department of Chemical and Biological Engineering, Seoul National University, Seoul 08826, Republic of Korea

^c Department of Chemistry, Seoul National University, Seoul 08826, Republic of Korea. E-mail: ysung@snu.ac.kr

^d Department of Chemical and Molecular Engineering, Hanyang University, Ansan 15588, Republic of Korea

† Electronic supplementary information (ESI) available. See DOI: 10.1039/c8nj04919j

550, and 650 °C to selectively generate Fe₂O₃ hollow structures, highly porous Fe₂O₃, and hierarchically structured shells consisting of Fe₂O₃ nanoplates, respectively, and these microcubes exhibited good performance as anodes for LIBs.¹⁶

Meanwhile, the thermolysis of MOFs under inert conditions has been achieved to form M/MO@C hybrid materials. For example, Xia *et al.* synthesized ZIF-67 of various sizes (from micrometers to nanometers) and then subjected them to thermolysis under inert conditions to form Co@C composites.¹¹ Co@C derived smaller MOF precursors presented higher oxygen reduction reaction (ORR) activities due to the larger exposed catalytic surface. Yang *et al.* reported MOF-5-derived ZnO quantum dots with a diameter of around 3.5 nm decorated in a porous carbon framework; the structure exhibited outstanding electrochemical performance as an anode material for LIBs.¹⁷ Lee *et al.* reported the control of oxidation states of MOF-derived manganese oxides with identical textural properties by controlling the thermolysis conditions; these oxides could be utilized as electrocatalysts for proving oxidation state-dependent ORR activity.¹⁸ In addition, the utilization of aliphatic ligands has resulted in controlled porosity in nanoporous metal oxide nanocrystals formed by thermolysis.¹⁷

Highly porous carbonaceous materials can be easily obtained from Zn-containing MOFs *via* thermolysis; here *in situ* Zn metal obtained from the carbothermic reduction of ZnO (ZnO(s) + C(s) → Zn(s) + CO(g)) vaporizes at high temperatures (typically > 900 °C).^{1,19–22} The microporosity and specific surface area (SSA) of MOF-derived carbon can be easily varied by varying the carbonization conditions, which have shown promising results as electrocatalysts for ORR, electrodes for supercapacitors, and CO₂ adsorbents.^{17,22–24}

To preserve the morphological advantages of MOFs, a two-step thermolysis that first proceeds under inert conditions to preserve the morphology, followed by low-temperature oxidation to form MO@C has been widely employed. Cho's group reported a Fe₂O₃ composite derived from MIL-88-Fe *via* a two-step thermolysis process: first, MIL-101 was heat-treated under N₂ at 500 °C to obtain FeO_x@C, which was then converted to morphology-preserved Fe₂O₃ by oxidation at 380 °C.²⁵ The spindle-like mesoporous Fe₂O₃ particles presented ultra-high capacitance as anode materials for LIBs. Ni/NiO@graphene composites were synthesized from Ni-based MOF, wherein Ni@graphene was first prepared by heat treatment under inert condition at 450 °C, followed by oxidation at 200 °C to generate Ni/NiO@graphene composites, which could be used as anode materials for LIBs and sodium-ion batteries.⁸ Xia *et al.* synthesized ZIF-67 inside a mesoporous CM, which was then subjected to a two-step heat treatment to form Co@CO₃O₄@CM composites; in these composites, the mesoporous carbon template facilitated mass transport, resulting in superior ORR activity.²⁶

Although fine-controlled MO and M/MO@C composites have shown promising electrochemical performance, a facile synthesis method combining all the aforementioned features is yet to be reported. In this regard, we have recently reported a facile synthesis approach that can control the porosity, content, and crystallinity of Cu/CuO/Cu₂O@C composites that are pseudomorphically

derived from HKUST-1 [Cu₃(btc)₂]. Phenol formaldehyde (PF) was vaporized and polymerized at two open Cu catalytic sites regularly spaced for every secondary building unit.²⁷ Crystallinity- and morphology-preserved PF@Cu-HKUST-1 was successfully achieved by vapor phase polymerization (VPP) and was then subjected to thermolysis to form Cu@C composites. CuO/Cu₂O@C composites were subsequently obtained by controlling of oxidation process. The size of the Cu@C particles could be easily adjusted by varying the carbonization conditions, and the amount of PF used for VPP was directly related to the Cu/CuO/Cu₂O nanoparticle content as well as the porosity of the carbon framework.

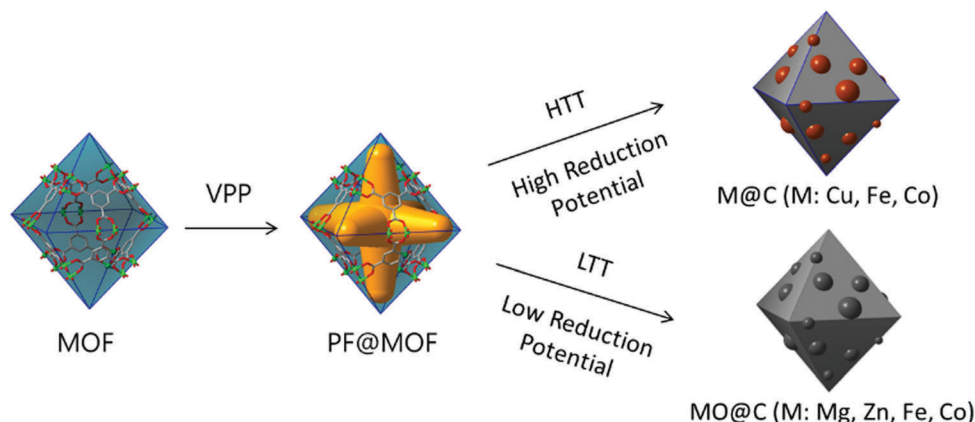
In this study, we explored the utilization of VPP method for MOFs of different metal sites with identical topology (M-HKUST-1, M: Cu and Zn, and M-MOF-74, M: Co, Fe, Mg) and MOF with small pore (3.4 Å, ZIF-8). The VPP of M-HKUST-1 (M: Cu and Zn) was successfully achieved, showing that site-specific polymerization can occur regardless of the metal center in the same topology. In addition, M-MOF-74 (M: Co, Fe, Mg) having a one-dimensional channel with a pore size of 10 Å was employed for VPP, resulting in morphology- and crystallinity-preserved PF@MOF-74 composites, thus confirming the applicability of VPP for MOFs with pore sizes larger than 10 Å. When ZIF-8 with a pore size of 3.4 Å was used for VPP, however, the morphology of ZIF-8 changed because of which phenol and formaldehyde cannot penetrate due to their narrow pore size.

PF@M-HKUST-1 and PF@M-MOF-74 were then subjected to thermolysis under inert conditions. The crystallinity was observed to vary depending on the reduction potential of the metal nodes and the carbothermic reduction reaction (MO + C → M + CO). Cu@C was obtained from Cu-HKUST-1, whereas Zn-HKUST-1 was transformed to ZnO@C initially and morphology-preserved carbon was eventually formed. For M-MOF-74, MgO@C was produced from Mg-MOF-74; on the other hand, Fe₂O₃@C was formed below 450 °C and Fe@graphite (Fe@G) and Fe₃C@G were finally produced from Fe-MOF-74 by prolonged high-temperature thermolysis. Similar trends were observed for Co-MOF-74; Co₃O₄@C was formed initially and Co/CoO@C was finally produced at higher temperatures. In addition, the porosity and content of M/MO/MC@C/G composites could be easily tuned by adjusting the amount of PF precursor. Furthermore, morphology-preserved and content- and porosity-optimized CuO@C composite was tested as an anode material for LIBs and were found to exhibit better electrochemical performance than less-optimized samples and CuO obtained from the direct oxidation of the parent MOF, and outstanding long-term stability with a remarkable specific capacity of 410 mA h g⁻¹ after 1000 cycles at a rate of 1000 mA g⁻¹.

Results and discussion

PF@MOF composites

VPP was first performed on activated M-HKUST-1 crystals (M: Cu and Zn) in a closed vessel under static vacuum at 100 °C for 24 h, as depicted in Scheme 1. According to the SEM images of pristine Cu-HKUST-1 and PF@Cu-HKUST-1 (Fig. 1a1 and a2), the



Scheme 1 Schematic illustration of pseudomorphic transformation of MOFs to M/MO@C composites via VPP and high and low-temperature thermolysis (HTT and LTT).

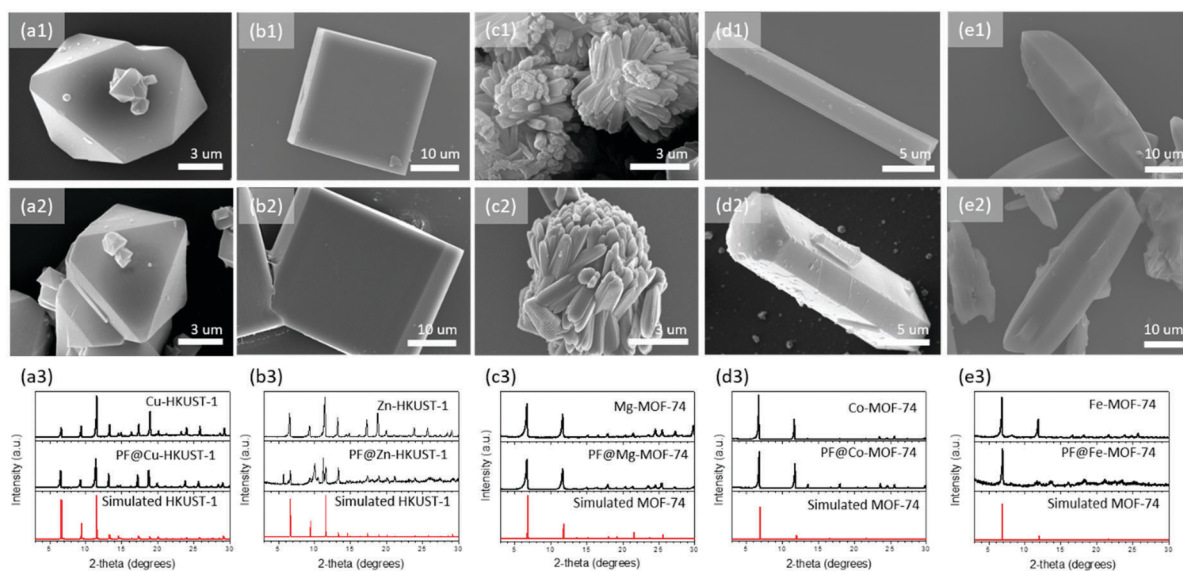


Fig. 1 Confirmation of shape-preserved PF@MOF after VPP with SEM images of as-synthesized MOFs (a1–e1) and PF@MOFs (a2–e2). Comparison of XRD patterns of MOFs and PF@MOFs (a3–e3).

octahedral morphology and smooth surface of the Cu-HKUST-1 crystals were preserved after VPP.

To identify the catalytic activity of different metal nodes, VPP was applied to different metal node with the same topology in Zn-HKUST-1. The cubic shape of Zn-HKUST-1 was well preserved after VPP (Fig. 1b1 and b2). The major XRD peaks of Zn-HKUST-1 were relatively well preserved after VPP, but several additional peaks were observed, which were probably attributed to degradation in the mechanical stability of Zn-HKUST-1 during VPP under static vacuum at 100 °C for 24 h (Fig. 1b3). The open Cu and Zn sites of HKUST-1 acted as catalysts for the site-specific polymerization of vaporized PF precursors under the given condition. It has been noted that mesoporous aluminosilicate materials are utilized as templates for the fabrication of mesoporous carbonaceous materials through the site-specific polymerization of vaporized PF precursors at acidic Al sites.^{28–30} Because polymerization starts at the catalytic

sites, the free volume of the porous preforms can ideally be occupied by the PF polymers, thus avoiding the formation of undesirable polymeric moieties on the surface of the preforms.³⁰ It was expected that other MOFs bearing open metal sites would be applicable to VPP. M-MOF-74 (M: Mg, Fe, and Co), which consists of hexagonal one-dimensional pore structures with open metal nodes, was utilized for preparing PF@MOF composites. Pristine M-MOF-74 showed linear hexagonal rod structures,^{31,32} which did not deform after VPP (Fig. 1c1 and c2, d1 and d2, and e1 and e2). PF@M-MOF-74 (M: Mg, Fe, and Co) presented characteristic XRD patterns corresponding to the parent MOFs, confirming that site-specific polymerization successfully occurred at the open metal sites within the micropores and that the crystallinities of the MOFs were preserved intact during VPP (Fig. 1c3, d3, and e3).

After VPP process, PF@MOF samples were further characterized by N₂ sorption and TGA measurements. All PF@MOF samples except (because Zn-HKUST-1 is readily collapsed during

N₂ sorption measurement, PF@Zn-KHUST-1 was not tested for N₂ sorption) presented almost nonporous features compared to MOFs, strongly suggesting that VPP occurring inside MOFs effectively closed the pores of MOFs (Fig. S1 and Table S1, ESI†). In addition, TGA was performed that around 8.9–13.4 wt% weight gains were identified for PF@MOF samples, strongly suggesting that polymerization successfully occurred inside pores of MOFs (Fig. S2, ESI†). Combined all characterization results including XRD, SEM, and N₂ sorption and TGA measurements, it should be clear that VPP occurred at the open metal catalytic sites located inside pores of MOFs, giving rise to shape-preserved and crystallinity-preserved PF@MOF composites.

According to the pore sizes of HKUST-1 (14 Å) and MOF-74 (10 Å), it was considered that the vaporized PF molecules readily entered the pore apertures and polymerized at the catalytic sites. Thus, ZIF-8, which had pore size of 10.9 Å that was accessible through small apertures with diameters of 3.4 Å, was tested for VPP to identify the pore size effect.³³ According to the SEM investigations, polymerization occurred on the surface of the polyhedral morphology of ZIF-8 (Fig. S3, ESI†). It was reported that the extraordinary flexibility of the ZIF-8 framework allowed molecules with sizes of 4–6 Å to enter the apertures.³⁴ Therefore, PF could enter the aperture of ZIF-8, but site-specific polymerization could not occur solely within the sodalite cage of ZIF-8.

M/MO/MC@C composite

PF@M-HKUST-1 (M: Cu and Zn) composites were first subjected to thermolysis under N₂ atmosphere at different temperatures.

When PF@Cu-HKUST-1 was heat-treated at a relatively low temperature (380 °C), most of the XRD peaks corresponded to Cu, while a few XRD peaks corresponding to CuO appeared (Fig. S4, ESI†). In contrast, when the thermolysis temperature was increased to 800 °C, only XRD peaks corresponding to Cu were observed (Fig. 2a1). This was probably because the standard reduction potential (SRP) of Cu²⁺ to Cu ($E^\circ = +0.337$ V) was positive; hence, Cu was preferentially formed under higher thermolysis temperatures.^{27,35} According to the SEM and TEM images (Fig. 2a2 and inset), the polyhedral shape of the resulting Cu@C composite resembled the morphology of the pristine MOF and Cu nanoparticles were well distributed within carbon framework, confirming that the morphology of the parent MOF was fully preserved even after thermolysis at high temperature. To control the crystal phase from Cu to CuO, mild oxidation at 200 °C was performed under air for 12 h. After the oxidation, a crystallinity change from Cu@C to CuO@C was observed in the XRD pattern (Fig. 2a1), without morphological change (Fig. 2a3, inset). Further TEM investigations revealed that CuO nanoparticles with a size less than 10 nm were spatially distributed throughout the specimen (Fig. 2a3). According to the Scherrer equation, the size of the Cu nanoparticles (60 nm) of Cu@C were much larger than that of the CuO nanoparticles (7.1 nm) of CuO@C. This was probably attributed to the stress-induced phase transformation from a cubic to a monoclinic unit cell,^{36–38} and it seemed that the Kirkendall effect occurred during oxidation, resulting in void spaces between the CuO nanoparticles.³⁹

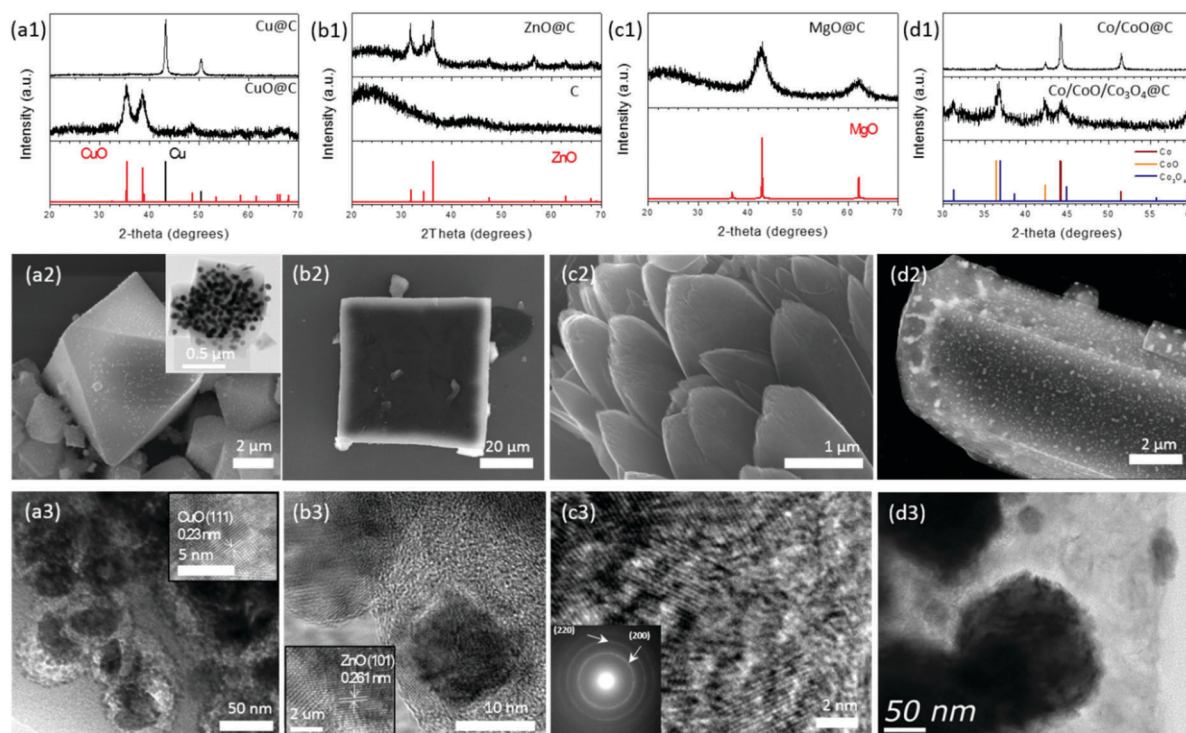


Fig. 2 XRD patterns of M/MO@C obtained by thermolysis and oxidation (a1–d1). SEM images of as-prepared Cu@C_{800 °C} (a2, inset: TEM image of Cu@C), ZnO@C_{700 °C} (b2), MgO@C_{800 °C} (c2), and Co/CoO@C_{800 °C} (d2). TEM images of CuO@C_{200 °C} (a3), ZnO@C (b3, inset: lattice fringe of ZnO), MgO@C (c3, inset: selected area electron diffraction pattern of MgO), and Co/CoO@C (d3).

A similar transformation trend was observed for PF@Zn-HKUST-1; initially, the formation of ZnO@C at a relatively low thermolysis temperature of 600 °C under N₂ atmosphere was confirmed by the XRD measurements, and crystal peaks corresponding to ZnO disappeared on further thermolysis at a higher temperature of 900 °C (Fig. 2b1). It is widely accepted that carbothermic reduction ($\text{ZnO (s)} + \text{C (s)} \rightarrow \text{Zn (s)} + \text{CO (g)}$) and subsequent vaporization of nano-sized metallic Zn proceeds at high temperatures (> 900 °C).^{1,19–22} Further, it has been widely reported that morphology-preserved carbonaceous materials with a high surface area can be prepared using Zn-containing MOFs; these materials can be used as CO₂ sorbents, electrocatalysts for ORR, and supercapacitors.^{17,22–24} According to the SEM image (Fig. 2b2), the cubic morphology of Zn-HKUST-1 was preserved in ZnO@C, and nano-sized ZnO nanocrystals with a *d*-spacing of 0.261 nm for the crystal fringe of (101) could be clearly observed within the CM (Fig. 2b3). In addition, the cubic shape was preserved for the carbon material prepared using high temperature thermolysis (Fig. S5, ESI†).

Further thermolysis was performed for the PF@M-MOF-74 (M: Mg, Fe, and Co) composites. According to XRD, crystalline MgO with a size of 3.2 nm was observed during the thermolysis of PF@Mg-MOF-74 at 800 °C (Fig. 2c1). Aggregated rods with sharp edges were observed by SEM and nano-sized MgO was embedded within the CM and the presence of polycrystalline MgO@C composites was confirmed by electron diffraction observations (Fig. 2c2, c3, and c3 inset).

Meanwhile, PF@Co-MOF-74 was subjected to thermolysis at a relatively low temperature of 500 °C, resulting in mixed crystals of CoO/Co₃O₄/Co@C (Fig. 2d1). Major crystals observed were CoO; nevertheless, XRD peaks corresponding to Co₃O₄ and Co were also observed. When a high thermolysis temperature of 800 °C was applied, Co crystals were formed as the major product and the peaks corresponding to CoO crystals had very small intensities. It was believed that the carbothermic reduction of Co oxides to Co metal occurred during high temperature thermolysis ($\text{Co}_3\text{O}_4 + \text{C} \rightarrow 3\text{Co} + 4\text{CO}$ and $\text{CoO} + \text{C} \rightarrow \text{Co} + \text{CO}$).

As expected, the rod shape morphology of Co-MOF-74 was preserved even after high-temperature treatment (Fig. 2d2), and TEM measurements showed the presence of Co nanocrystals spatially distributed throughout the CM (Fig. 2d3).

Lastly, PF@Fe-MOF-74 was subjected to thermolysis at various temperatures. When the composite was treated at a low temperature of 450 °C, only $\gamma\text{-Fe}_2\text{O}_3$ nanocrystals with size of 4.5 nm (as determined by the Scherrer equation) were formed (Fig. 3a). When the thermolysis proceeded at 600 °C, metallic Fe with a size of *ca.* 60 nm was the only product (Fig. 3a); on the other hand, XRD patterns corresponding to Fe₃C and Fe appeared when further thermolysis was performed at 800 °C (Fig. S6, ESI†). It was possible that the carbothermic reduction of $\gamma\text{-Fe}_2\text{O}_3$ ($\gamma\text{-Fe}_2\text{O}_3 + \text{C} \rightarrow 2\text{Fe} + 3\text{CO}$) formed metallic Fe, which further underwent carbide formation to provide Fe₃C at the higher temperature (800 °C).⁴⁰ The crystallinity transformation will be discussed in detail in the next section.

According to the SEM images, $\gamma\text{-Fe}_2\text{O}_3$ @C presented a smooth rod shape, identical to the parent Fe-MOF-74, thus confirming that the morphological feature of the pristine MOF was preserved after VPP and thermolysis (Fig. 3b). TEM investigations clearly confirmed that tiny $\gamma\text{-Fe}_2\text{O}_3$ nanocrystals with a size less than 5 nm and a crystalline fringe of (311) with a *d*-spacing of 0.251 nm were spatially distributed throughout the one-dimensional rod-shaped CM (Fig. 3c). On the other hand, the SEM image of the Fe@C sample still showed a one-dimensional rod shape but clearly presented a rough surface with white dots, unlike the smooth surface of the $\gamma\text{-Fe}_2\text{O}_3$ @C sample (Fig. 3d). Further TEM investigation indicated the broad size distribution of Fe nanoparticles within the one-dimensional carbon rod (Fig. 3e).

When we carefully observed the edges of the Fe@C composite, several hollow holes of diameters less than 50 nm were clearly observed and graphene layers with a thickness of around 10 nm formed hollow structures (*d*-spacing was measured as 0.34 nm; Fig. 3f and inset). Thus, it was reasonable to assume that the Fe nanoparticles formed *in situ* first catalyzed to form graphene

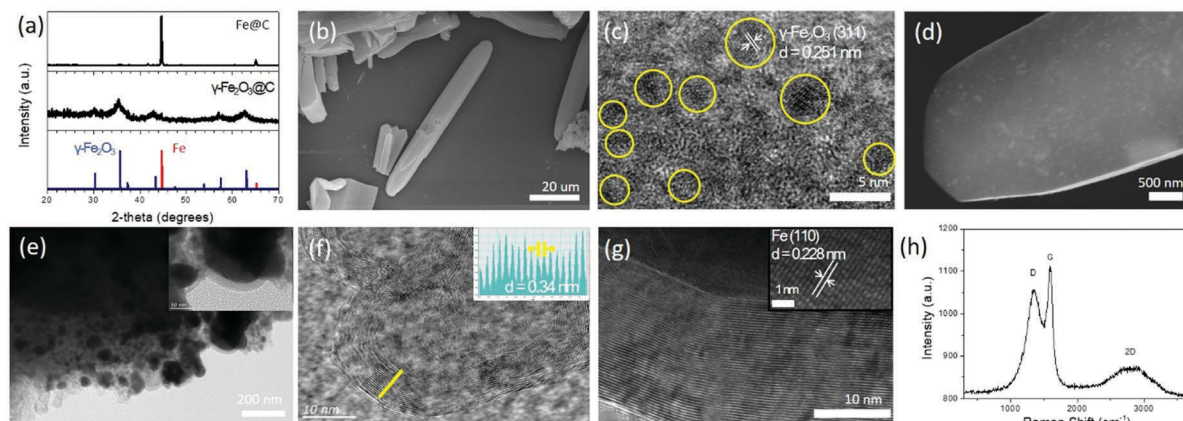


Fig. 3 XRD patterns of $\gamma\text{-Fe}_2\text{O}_3$ @C and Fe@G derived from PF@Fe-MOF-74 under different thermolysis conditions (a). SEM (b) and TEM (c) images of $\gamma\text{-Fe}_2\text{O}_3$ @C. SEM (d) and TEM (e) images of Fe@G. TEM image of hollow graphite (f) and *d*-spacing of graphitic layers (inset of f). TEM image (g) of Fe@G with crystalline fringe of (110) of Fe nanocrystals (inset of g). Raman spectra of hollow graphite after acid treatment of Fe@G (h).

layers on the surface and aggregated to form larger particles during thermolysis, which eventually formed hollow graphene structures. On the other hand, large Fe particles were wrapped with thicker graphene layers than the hollow structures (Fig. 3f and g). Graphene layers with thicknesses of around 20 nm were conformally coated on the shaped Fe nanoparticles and characteristic (110) crystalline planes with a *d*-spacing of 0.228 nm were clearly identified in the Fe nanoparticles (Fig. 3g and inset).

To investigate the graphitic feature of Fe@C, the Fe component of the composite was selectively removed by acid treatment and XRD and Raman measurements were performed. According to the XRD results (Fig. S7, ESI†), a diffraction peak at *ca.* 26°, corresponding to the (002) plane of the graphitic domain, clearly appeared, confirming that Fe nanoparticles catalyzed the formation of graphitic layers on the surface. In addition, the Raman spectrum showed a well-developed G band (*ca.* 1580 cm⁻¹) with an *I_D/I_G* ratio of 0.87 and a broad band ranging from 2500 to 2800 cm⁻¹, corresponding to the 2D band, which are characteristic features of sp² graphitic materials (Fig. 3h).⁴¹ Therefore, the Fe@C sample is hereafter denoted as Fe@G.

Thermodynamic calculation for M/MO/MC@C

In this section, we discuss the crucial factors controlling the crystallinity of morphology-preserved M/MO/MC@C/G composites prepared *via* VPP and thermolysis. First, the standard reduction potential (SRP) should be considered to be a pivotal factor governing the final crystallinity phase of the MOF-derived composites obtained by thermolysis under inert conditions. Das *et al.* reported that metal ions with an SRP higher than -0.27 V always presented pure metal nanoparticles, whereas those with an SRP lower than -0.27 V presented metal oxide nanoparticles, which were dispersed within a CM.⁴⁰ Regarding this aspect, the SRP values of the metal ions used in this study, Mg²⁺, Zn²⁺, Fe²⁺, Co²⁺, and Cu²⁺, were -2.69, -0.76, -0.44, -0.27, and 0.33 V, respectively (Table 1). According to our results, the trend of products obtained by thermolysis under inert conditions was similar to that reported by Das *et al.*, except for Co and Fe-MOF-74. CoO was a major product of

the thermolysis performed at a temperature of 500 °C and transformed to Co nanocrystals when thermolysis was performed at a higher temperature of 800 °C (Fig. 2d1). In addition, γ-Fe₂O₃ was first formed at a low thermolysis temperature of 450 °C and was transformed to Fe nanocrystals at 600 °C and Fe/Fe₃C nanocrystals on further thermolysis at 800 °C (Fig. 3a and Fig. S6, ESI†).

In this regard, another factor affecting crystallinity change should be considered, which is carbothermic reduction. In this reaction, carbon is utilized as a reducing agent to reduce substances such as metal oxides; the reaction can generally be described as follows: MO(s) + C(s) → M(s) + CO(g) (gaseous product is sometimes carbon dioxide).⁴² A well-known example is silicon production *via* the carbothermic reduction of SiO₂, which is usually performed above 1100 °C.⁴³ To predict whether carbothermic reduction with metal oxides of MgO, ZnO, Fe₂O₃, CoO, and CuO occurred, thermodynamics calculations for free energy change as a function of temperature were performed, which was described in detail in the ESI† (Note 1 and Table S1). For MgO, the value of free energy change was positive in for temperatures up to 1000 °C (Fig. 4a); MgO was the only product of thermolysis because of its very low SRP value of -2.69 V (Table 1). A similar trend was obtained for ZnO, but its free energy change was a very small positive value at high temperature. Accordingly, numerous studies reported the *in situ* formation of pure metallic Zn metal *via* the carbothermic reduction of ZnO@C, which eventually vaporizes to produce carbonaceous materials (Fig. 4b).^{1,19–22}

The carbothermic reduction of Fe₂O₃ (2Fe₂O₃(s) + 3C(s) → 4Fe + 3CO₂(g)) has been widely utilized for iron ore smelting.⁴⁴ As expected, the free energy change for pure Fe nanocrystals was -697.5 kJ mol⁻¹ at 600 °C (Fig. 4c), which confirmed that γ-Fe₂O₃ transformed to pure Fe nanoparticles after thermolysis at 600 °C (Fig. 3a). In addition, the free energy change for the carbothermic reduction of CoO (CoO(s) + C(s) → Co(s) + CO(g)) became negative just above 600 °C (Fig. 4d), which confirmed that CoO transformed to pure Co nanocrystals after thermolysis at a temperature of 800 °C (Fig. 2d1). Lastly, the free energy change for the carbothermic reduction of CuO (CuO(s) + C(s) → Cu(s) + CO(g)) showed a large negative value throughout the temperature range, suggesting that only pure Cu nanocrystals were formed after high-temperature treatment (Fig. 4e).

The other factor affecting the crystallinity was carbide formation. According to our results, the XRD patterns corresponding to Fe₃C appeared after higher temperature (800 °C) thermolysis reaction. It was confirmed that Fe₃C formation (3Fe(s) + C → Fe₃C(s)) was favorable, as determined by the free energy change calculation (Fig. 4c).

Textural features of M/MO@C composites

Nitrogen sorption measurements were performed to obtain the textural features such as SSA, pore volume, and pore size distribution (PSD) of the as-prepared M/MO@C samples. Characteristic type I isotherms were observed for all Cu@C, ZnO@C, C derived from ZnO@C, MgO@C, γ-Fe₂O₃@C, Fe@G, and Co/CoO@C samples, indicating that microporosity originated

Table 1 Standard reduction potentials (SRPs) and final crystalline products of PF@MOF composites after thermolysis at various temperatures

Sample	Reduction potential (eV)	Temperature (°C)	Product
PF@Cu-HKUST-1	+0.337	380	Cu/CuO@C
		800	Cu@C
PF@Zn-HKUST-1	-0.76	600	ZnO@C
	-0.76	900	C
PF@Mg-MOF-74	-2.69	800	MgO@C
PF@Co-MOF-74	-0.27	500	Co/CoO/Co ₃ O ₄ @C
		800	Co/CoO@C
PF@Fe-MOF-74	-0.44	450	γ-Fe ₂ O ₃ @C
		600	Fe@C
		800	Fe/Fe ₃ C@C

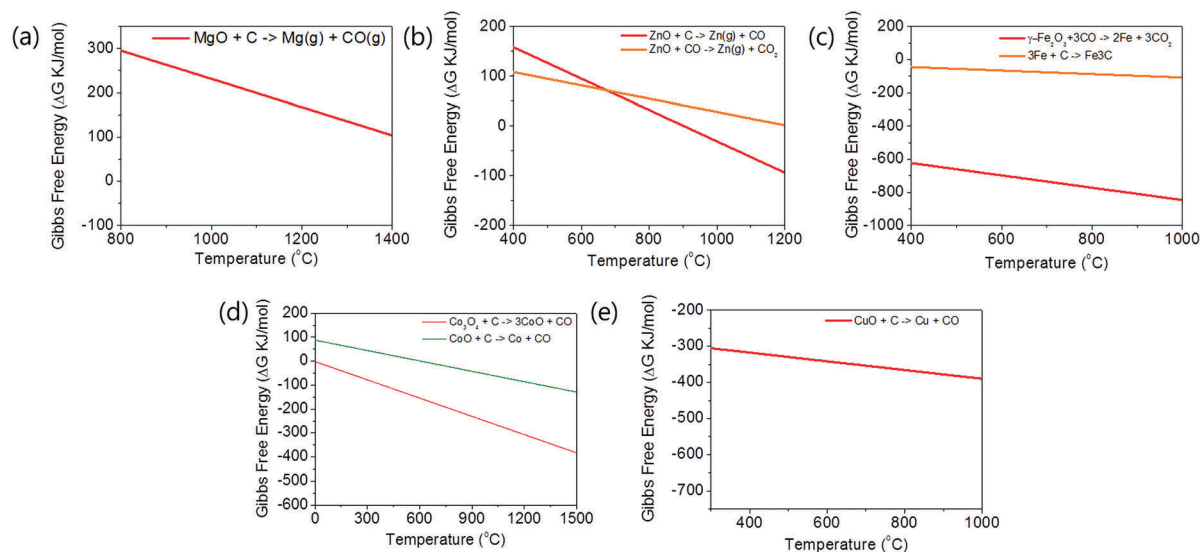


Fig. 4 Free energy diagrams for carbothermal reduction of MgO (a), ZnO (b), Fe_2O_3 and Fe (c), Co_3O_4 and CoO (d), and CuO (e).

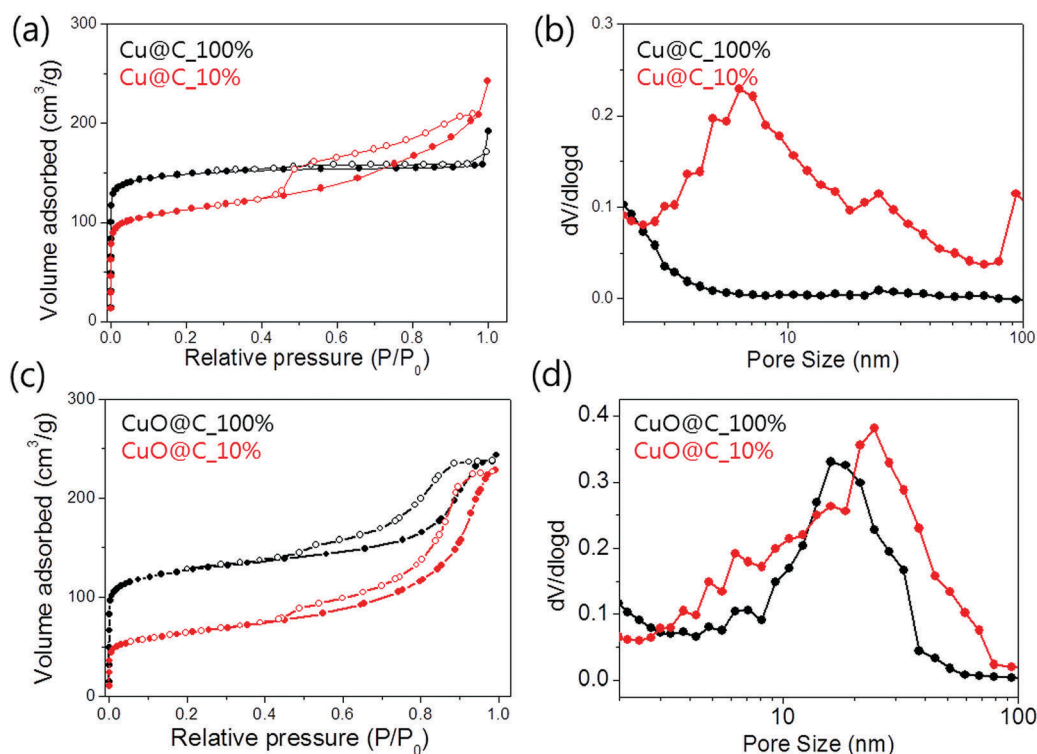


Fig. 5 N_2 adsorption isotherms of Cu@C and CuO@C with different carbon contents (a and c) at 77 K. Barrett–Joyner–Halenda plot of Cu@C and CuO@C with different carbon contents (b and d).

from the CM (Fig. 5 and Fig. S8–S11, ESI[†]). The SSAs of the M/MO@C composites determined by the BET method and their pore volumes are listed in Table 2; all samples had values in the range of several hundreds of $\text{m}^2 \text{g}^{-1}$, confirming the well-developed porosity of the M/MO@C composites. Among them, C derived from ZnO@C exhibited an ultrahigh SSA of $1145 \text{ m}^2 \text{g}^{-1}$ (Fig. S8, ESI[†] and Table 2) due to high temperature thermolysis, which agreed with previous results.^{1,19–22} In addition, well-developed

mesopores with sizes ranging from several nanometers up to around 20 nm were identified for C, which probably originated from the disappearance of nanosized ZnO nanoparticles with sizes of ca. 15 nm (as determined by the Scherrer equation; Fig. 2b1).

Unexpected mesoporosity development was observed for higher temperature thermolysis products such as Fe@G and Fe/Fe₃C@C composites (Fig. S11, ESI[†]). This might be related to the carbothermic reduction ($\text{MO(s)} + \text{C(s)} \rightarrow \text{M(s)} + \text{CO(g)}$) of

Table 2 Textural properties of M/MO@C composites

Sample	S_{BET}^a ($\text{m}^2 \text{g}^{-1}$)	V_{tot}^a ($\text{cm}^3 \text{g}^{-1}$)	V_{micro}^b ($\text{cm}^3 \text{g}^{-1}$)	M/MO ^c (wt%)
Cu@C_100%	584.0	0.26	0.23	37.5
Cu@C_10%	422.7	0.35	0.12	62.7
CuO@C_100%	478.66	0.37	0.16	39.1
CuO@C_10%	228.06	0.35	0.04	73.5
ZnO@C	432	0.197	0.173	—
C	1145	0.622	0.414	0
MgO@C	1255.9	0.67	0.54	34.7
Co/CoO/Co ₃ O ₄ @C	240	0.25	0.08	—
Co/CoO@C	206	0.14	0.08	—
γ -Fe ₂ O ₃ @C_100%	174.32	0.11	0.06	44.5
γ -Fe ₂ O ₃ @C_10%	95.5	0.067	0.039	58.3
Fe@C	357	0.23	0.12	—
Fe/Fe ₃ C@C	208	0.24	0.05	—

^a SSA and total pore volume obtained by BET method and at $P/P_0 = 0.99$, respectively. ^b Calculated by the t -plot method. ^c Measured by TGA.

both samples and because higher temperature thermolysis involved more oxygen consumption of the composites, eventually resulting in the formation of mesopores in the resulting composites.

On the other hands, the SSA, pore volume, and PSD of M/MO@C could be varied by varying the amount of PF precursor used for VPP, which simultaneously influenced the weight percentage of M or MO in the composites. First, Cu@C was prepared using different PF amounts of 100% and 10%, denoted as Cu@C_100% and Cu@C_10%, respectively. Compared to Cu@C_100%, Cu@C_10% showed a combined type I and IV adsorption isotherm, representing microporosity and mesoporosity, respectively (Fig. 5a). Due to use of a small PF precursor amount in Cu@C_10%, a PSD centered at *ca.* 6.2 nm was developed; on the other hand, the SSA of Cu@C_10% was 426.26 $\text{m}^2 \text{g}^{-1}$, reduced from 588.58 $\text{m}^2 \text{g}^{-1}$ for Cu@C_100%, probably owing to the fewer carbon moieties in the composite (Fig. 5b and Table 2). In addition, the weight percentage of Cu for the Cu@C_100% and Cu@C_10% samples changed to 37.5 and 62.7 wt%, respectively, because of the use of a small PF precursor amount for Cu@C_10% (Fig. S12, ESI† and Table 2).

In addition, CuO@C_100% and CuO@C_10% were prepared *via* mild oxidation of Cu@C_100% and Cu@C_10%. The resulting CuO@C_100% and _10% both represented type I isotherms, inferring that microporosity originating from the CM of the parent materials was well preserved even after oxidation (Fig. 5c). Interestingly, CuO@C_100% and _10% both samples also showed type IV isotherms, with PSDs centered at 15.9 nm and 24.43 nm, respectively (Fig. 5c and d). The mesoporosity of CuO@C_10% was reasonable because the parent Cu@C_10% already presented mesoporosity (Fig. 5b); on the other hand, the mesoporosity of CuO@C_100% was unexpected due to lack of mesoporosity in its parent sample. Notably, during oxidation, Cu nanoparticles with a size of *ca.* 60 nm were transformed into tiny CuO nanoparticles with size of around 4.5 nm (Fig. 2a2 and a3), and some void spaces were observed by TEM (Fig. 2a3). This was probably due to the

reduced particle size induced by transformation from a cubic to a monoclinic unit cell as well by the formation of void spaces due to the Kirkendall effect during oxidation,^{36–39} from which the mesoporosity of CuO@C_100% may have originated. In addition, the SSAs of CuO@C_100% and _10% were 478.66 and 228.06 $\text{m}^2 \text{g}^{-1}$, respectively; the smaller SSA for CuO@C_10% could be attributed to the smaller CM, which was also confirmed by the TGA results of 39.1 wt% and 73.5 wt% of CuO, respectively (Table 2 and Fig. S13, ESI†).

This process could be applied to other MOFs. For example, the textural features and weight percentage of γ -Fe₂O₃@C were adjusted by varying the PF precursor amount during VPP. The γ -Fe₂O₃@C_10% sample was prepared using 10% PF precursor, whereas γ -Fe₂O₃@C, as already mentioned, is hereafter denoted as γ -Fe₂O₃@C_100%. γ -Fe₂O₃@C_10% presented a characteristic type I isotherm, indicating that microporosity originated from the CM (Fig. S11, ESI†). On the other hand, the SSA and micropore volume of γ -Fe₂O₃@C_10% were 95 $\text{m}^2 \text{g}^{-1}$ and 0.039 cc g^{-1} , respectively, which were smaller than those of γ -Fe₂O₃@C_100%, and the weight percentage of γ -Fe₂O₃ for γ -Fe₂O₃@C_10% was 58.3 wt%, larger than that (44.5 wt%) of γ -Fe₂O₃@C_100% because of the less-developed CM (Table 2 and Fig. S14, ESI†). Therefore, the SSA, micropore volume, and weight percentage of M or MO of the M/MO@C composites could be easily varied by adjusting the amount of PF precursor used during VPP; this is a useful method to fabricate advanced materials for various applications.

Electrochemical performance

Among the MOF-derived M/MO@C composites, CuO@C has been applied as anode materials for LIBs. CuO has been widely investigated as a next-generation anode material for LIBs because of its advantages over conventional graphite anode (theoretical capacity of 372 mA h g^{-1}) in terms of a high theoretical capacity of 674 mA h g^{-1} , relatively low cost, environmental friendliness, and other factors.^{14,25,45–50} These transitional metal oxides, however, suffer from several issues, including large volume changes, resulting in pulverization of the electrode material and eventually capacity fading during charge/discharge, and relatively low electrical conductivity, causing additional capacity fading, especially at high current densities.^{25,45} To overcome these issues, porous and conductive materials are incorporated in the metal oxide anodes to mitigate the large volume changes occurring during charge/discharge and increase the electrical conductivity, respectively.^{25,45} In this regard, porosity-controlled and conductive carbon-clad CuO@C series are good candidates for next-generation anodes of LIBs.

Galvanostatic lithiation/delithiation of the CuO@C_100% and _10% samples and of CuO derived from the direct oxidation of Cu-HKUST-1 was first performed in a voltage range of 0.01–3.0 V (Fig. 6a) at a current density of 100 mA g^{-1} . CuO@C_10% presented first discharge and charge capacities of 1027 and 541.4 mA h g^{-1} , respectively, with a low Coulombic efficiency (CE) of 52.7%, ascribed to the decomposition of the electrolyte, which eventually resulted in the irreversible

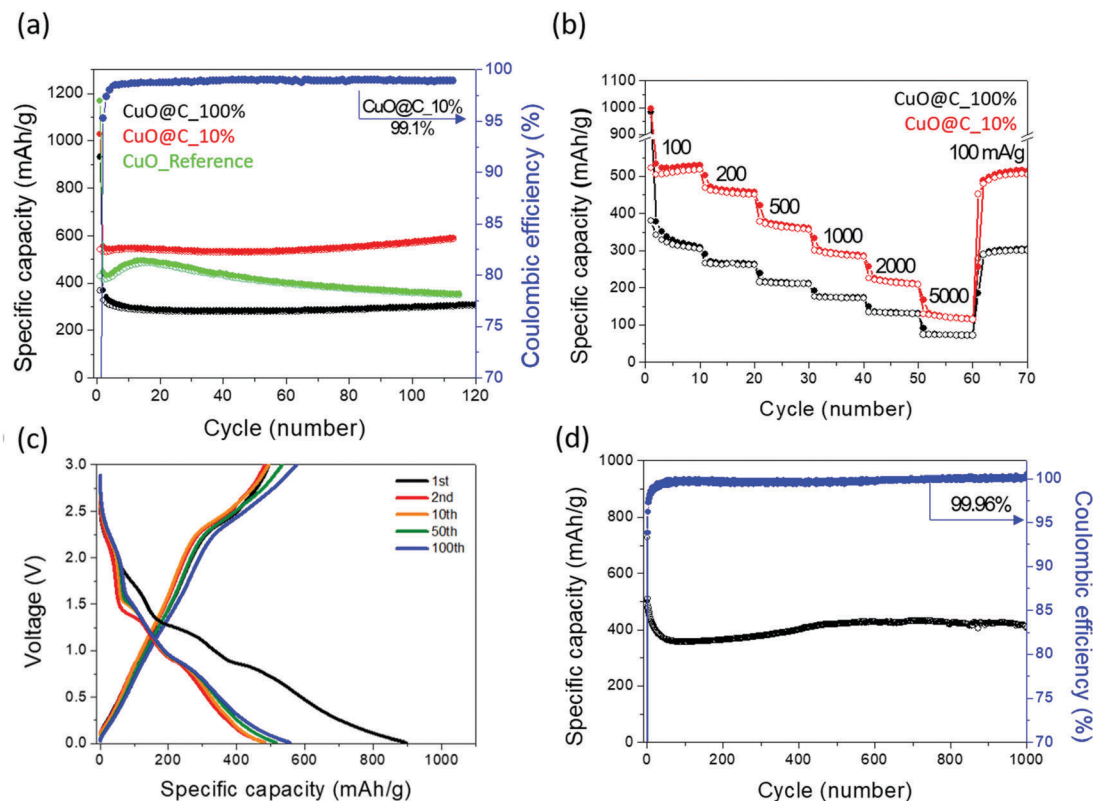


Fig. 6 Cycling property and rate performance of CuO@C_100 and _10% samples (a and b), voltage profile of CuO@C_10% (c) and long-term stability of CuO@C_10% at 1000 mA g⁻¹ over 1000 cycles (d).

formation of a solid electrolyte interphase (SEI) layer, commonly observed in metal oxide anode materials of LIBs.^{45–51}

CuO@C_10% presented an excellent capacity of 586.3 mA h g⁻¹ after 110 cycles, with a very high CE of 98.9% (Fig. 6a). When considering the weight percentage of CuO (73.5 wt%, see Table 2) in CuO@C_10%, the capacity value was higher than theoretical capacity of 73.5% of CuO (672 mA h g⁻¹), which may be attributed to the lithium-ion storage capacity of the CM. CuO@C_10% exhibited a much higher capacity than CuO@C_100% (303.9 mA h g⁻¹ over 110 cycles) probably due to its well-defined mesoporosity and higher CuO content (Fig. 6a). In addition, the CuO@C_10% sample showed a much more stable cycling performance as well as a higher capacity than that (356 mA h g⁻¹) of CuO derived from the direction oxidation of Cu-HKUST-1 (Fig. 6a), which decreased rapidly after the 20th cycle. In addition, CuO@C_10% exhibited a good cycling stability and higher capacity values than CuO@C_100% at rapid charge/discharge rates of up to 5000 mA g⁻¹ and recovered a similar capacity value at a low current density of 100 mA h g⁻¹, indicating the excellent rate capability of the CuO@C_10% sample (Fig. 6b).

The voltage profile for CuO@C_10% at 100 mA g⁻¹ was plotted in the Fig. 6c, showing that after 1st cycle, high coulombic efficiencies were well maintained up to 100 cycles. The long-term stability of CuO@C_10% was investigated at a rate of 1000 mA g⁻¹. The first discharge and charge capacities were 725.5 and 500.6 mA h g⁻¹, respectively, with a CE of 69%.

Meanwhile, the capacity continuously decreased to 358 mA h g⁻¹ until the 80th cycle, which could be attributed to the formation of the unstable SEI layer during high-rate charge/discharge (Fig. 6d). The specific capacity, however, increased up to 415 mA h g⁻¹ in the 450th cycle and was maintained until the 1000th cycle. Such remarkable long-term stability with outstanding specific capacity has rarely been achieved in anode materials composed of transitional metal oxides and probably originated from the structural integrity of the CuO@C composite, which consisted of spatially distributed CuO nanocrystals embedded within electrically conductive carbonaceous materials.

Conclusions

In this study, we have shown a facile synthesis method for adjusting the porosity, content, and crystallinity of M/MO@C composites that were pseudomorphically derived from MOFs (Cu- and Zn-HKUST-1 and Mg-, Co-, and Fe-MOF-74) *via* VPP and thermolysis. Site-specific gas-phase polymerization occurring at the open metal sites of MOFs with pore sizes larger than 10 Å was successfully achieved by VPP, providing morphology- and crystallinity-preserved PF@MOF composites. At this stage, the amount of PF precursor could be controlled, which was directly and simultaneously related to the porosity and content of the resulting M/MO@C composites after the thermolysis of PF@MOFs.

PF@M-HKUST-1 (M: Cu and Zn) and PF@M-MOF-74 (M: Co, Fe, and Mg) were then subjected to thermolysis under inert conditions. The crystallinity of M/MO@C was varied depending on the SRP of the metal nodes and carbothermic reduction reactions. An SRP greater than -0.27 V (Cu^{2+}) formed Cu@C, but metal ions with an SRP lower than -0.76 V (Mg^{2+} and Zn^{2+}) formed metal oxide nanoparticles (MgO@C and ZnO@C). In contrast, the SRP values of -0.44 and -0.27 for Fe^{2+} and Co^{2+} , respectively, provided different crystallinities depending on the thermolysis temperature; the major products for lower temperature (450 – 500 °C) thermolysis were metal oxides (*i.e.*, γ - Fe_2O_3 and CoO), while those for high temperature thermolysis (600 – 800 °C) were metal and metal carbide@C (Fe, Fe_3C , and Co). Such crystallinity transformation originated from carbothermic reduction and carbide formation during high temperature thermolysis. Furthermore, morphology-preserved and content- and porosity-optimized CuO@C composites were tested as anode materials for LIBs, and they exhibited superior electrochemical performance than less-optimized sample and CuO obtained from the direct oxidation of the parent MOF, and outstanding long-term stability with a remarkable specific capacity of 410 mA h g^{-1} after 1000 cycles at a rate of 1000 mA g^{-1} .

Experimental

Materials and methods

$\text{Zn}(\text{NO}_3)_2 \cdot 6\text{H}_2\text{O}$, $\text{Cu}(\text{NO}_3)_2 \cdot 2.5\text{H}_2\text{O}$, and $\text{FeCl}_3 \cdot 4\text{H}_2\text{O}$ were purchased from Sigma Aldrich. $\text{Co}(\text{CH}_3\text{CO}_2)_2 \cdot 4\text{H}_2\text{O}$, 2-methylimidazole, 1,3,5-benzenetriacetate (BTC), and 2,5-dihydroxyterephthalic acid (DOBDC) were purchased from Tokyo Chemical Industry (TCI). *N,N*-Dimethyl formamide (DMF), acetonitrile (MeCN), ethanol (99.999%), and methanol were purchased from Daejung. Ethanol (99.99%) and tetrahydrofuran (THF) were purchased from Samchun Chemical.

Zn-HKUST-1⁵². 268 mg (0.9 mmol) $\text{Zn}(\text{NO}_3)_2 \cdot 6\text{H}_2\text{O}$ was dissolved in 15 mL DMF. After 15 min, 128 mg (0.6 mmol) BTC was added and stirred for 15 min. The mixed solution was sealed in a 20 mL glass vial and then placed in an oil bath at 80 °C for 16 h. The obtained product was washed in both DMF and MeCN 3 times and immersed in MeCN for 1 day.

Cu-HKUST-1⁵³. 500 mg (2.14 mmol) $\text{Cu}(\text{NO}_3)_2 \cdot 2.5\text{H}_2\text{O}$ was dissolved in 15 mL DMF. After 15 min, 126 mg (1.42 mmol) BTC was added and stirred for 15 min. The mixed solution was sealed in a 20 mL glass vial and then placed in an oil bath at 80 °C for 16 h. The obtained product was washed in both DMF and MeCN 3 times and immersed in MeCN for 1 day. The product was then heated to 80 °C under vacuum for 12 h to activate the pores and open metal sites. We could observe that the original light blue powder changed to a deep blue color.

ZIF-8³⁴. 300 mg $\text{Zn}(\text{NO}_3)_2 \cdot 6\text{H}_2\text{O}$ and 660 mg 2-methylimidazole were successively dissolved in 14.2 mL methanol. The mixture was sealed in a 20 mL glass vials and placed in 120 °C for 16 h. The product was washed in methanol 3 times and immersed in methanol for 1 day.

Mg-MOF-74⁵⁵. 186 mg $\text{Mg}(\text{NO}_3)_2 \cdot 6\text{H}_2\text{O}$ and 40 mg DOBDC were sequentially dissolved in a solution containing 17.6 mL DMF, 1.2 mL EtOH, and 1.2 mL deionized (DI) water and the mixed solution was placed in an oil bath at 125 °C for 24 h after sealing it in a 20 mL vial. After the reaction, methanol was used to remove the mother liquor and vacuum was applied at 80 °C to activate the pores.

Co-MOF-74⁵⁶. 400 mg $\text{Co}(\text{CH}_3\text{CO}_2)_2 \cdot 4\text{H}_2\text{O}$ was dissolved in 10 mL H_2O . At the same time, 319 mg DOBDC was dissolved in 10 mL THF. Both solutions were mixed in a Teflon tape autoclave and then placed in an oven 100 °C oven for 2 days. The obtained product was washed in EtOH 3 times and immersed in EtOH for 1 day. The product was then heated to 80 °C under vacuum for 6 h to activate the pores and open metal sites.

Fe-MOF-74²⁸. 263 mg $\text{FeCl}_3 \cdot 4\text{H}_2\text{O}$ was dissolved in a solution containing 13.55 mL DMF, 0.725 mL iso-propanol, and 0.725 mL H_2O . After stirring for 15 min, 135 mg DOBDC powder was dissolved for 15 min. The mixed solution was sealed in a 20 mL glass vial and then placed in an oil bath at 105 °C for 24 h. The obtained product was washed in DMF and EtOH 3 times and immersed in EtOH for 1 day. The product was activated at 80 °C under static vacuum.

PF@MOF. VPP was performed in a 500 mL glass reactor. For the HKUST-1 samples, 200 mg activated HKUST-1, 340 mg phenol, and 260 mg paraformaldehyde were placed in the glass reactor. After sealing the reactor, the reaction was performed at 100 °C for 24 h. For the MOF-74 series, 200 mg phenol and 150 mg paraformaldehyde were used with the other parameters the same. PF@Cu-HKUST-1 and PF@Fe-MOF-74 samples are denoted as PF@Cu-HKUST-1_100% and PF@Fe-MOF-74_100%, respectively, and when the amount of PF is used 10% relative to 100%, they are then denoted as PF@Cu-HKUST-1_10% and PF@Fe-MOF-74_10%, respectively.

Synthesis of M/MO@C composites. As-synthesized PF@MOF composites were subjected to thermolysis under nitrogen atmosphere at specific temperatures ranging from 380 to 1000 °C at a heating rate of 4.5 °C min^{-1} and maintained for 3 h.

Synthesis of CuO@C from Cu@C. Mild oxidation at 200 °C for 12 h under air for Cu@C was performed to synthesize CuO@C.

Synthesis of reference CuO. Reference CuO was obtained by the calcination of Cu-HKUST-1 at 400 °C for 3 h under air.

Characterizations

Low-temperature nitrogen adsorption-desorption isotherms were measured at -196 °C using an adsorption volumetric analyzer (BEL MINI, BEL Inc., Japan). All MOF and PF@MOF samples were degassed at 100 °C for 24 h under static vacuum before the adsorption measurements, and the M/MO@C samples were degassed at 180 °C for 18 h under static vacuum. The SSA was determined using the Brunauer-Emmet-Teller (BET) method in the relative pressure range of 0.05 – 0.20 . The total pore volume was estimated from the amount of gas adsorbed at the relative pressure $P/P_0 = 0.99$. Micropore volumes were calculated from the corresponding isotherms

using the *t*-plot method. Scanning electron microscopy (SEM) images were recorded on a SEMIRON 5000 microscope (SERON Technologies Inc., Korea) at an accelerating voltage of 20 kV. Thermogravimetric analysis (TGA) was performed using an SDT Q600 device (TA Instruments Inc.), and transmission electron microscopy (TEM) images were recorded on a JEM-2100F microscope (JEOL Inc.).

Electrochemical measurements

The electrochemical performance was evaluated using CR2032-type coin cell fabricated using the prepared samples as the anode, Li metal foil as the anode, 1.0 M LiPF₆ solution in ethylene carbonate/diethyl carbonate (1:1 vol, Panatech, Korea) as the electrolyte, and a polypropylene membrane (SK innovation, Korea) as the separator. The working electrode was fabricated using a slurry composed of active materials, Super P, and polyvinylidene fluoride dispersed in *N*-methyl-2-pyrrolidinone (Sigma Aldrich) in a weight ratio of 80:10:10 and coated onto a copper foil using the Dr Blade method. The coin cells were assembled in a glove box filled with argon gas, and their electrochemical performance was evaluated using a WBCS 3000 battery cycler system (WonATech Corp., Korea) in a voltage range of 0.01–3.0 V (*versus* Li/Li⁺) at 25 °C using a thermostat.

Conflicts of interest

There are no conflicts to declare.

Acknowledgements

This work was supported by the basic science research program of the National Research Foundation (2016R1D1A1B03930258), the Korea Basic Science Institute under the R&D program (Scientific Instruments Reliability Assessment Project No. D36620) supervised by the Ministry of Science and ICT, and the Institute of Basic Science (IBS-R006-A2) in Republic of Korea.

References

- W. Xia, A. Mahmood, R. Zou and Q. Xu, *Energy Environ. Sci.*, 2015, **8**, 1837–1866.
- W. Chaikittisilp, K. Ariga and Y. Yamauchi, *J. Mater. Chem. A*, 2013, **1**, 14–19.
- D. Tian, X. L. Zhou, Y. H. Zhang, Z. Zhou and X. H. Bu, *Inorg. Chem.*, 2015, **54**, 8159–8161.
- W. Chen, R. B. Rakhi, M. N. Hedhili and H. N. Alshareef, *J. Mater. Chem. A*, 2014, **2**, 5236–5243.
- D. Yuan, J. Chen, S. Tan, N. Xia and Y. Liu, *Electrochem. Commun.*, 2009, **11**, 1191–1194.
- L. Wang, Y. Han, X. Feng, J. Zhou, P. Qi and B. Wang, *Coord. Chem. Rev.*, 2016, **307**, 361–381.
- Z. Y. Sui, P. Y. Zhang, M. Y. Xu, Y. W. Liu, Z. X. Wei and B. H. Han, *ACS Appl. Mater. Interfaces*, 2017, **9**, 43171–43178.
- F. Zou, Y.-M. Chen, K. Liu, Z. Yu, W. Liang, S. M. Bhaway, M. Gao and Y. Zhu, *ACS Nano*, 2016, **10**, 377–386.
- J.-L. Niu, G.-X. Hao, J. Lin, X.-B. He, P. Sathishkumar, X.-M. Lin and Y.-P. Cai, *Inorg. Chem.*, 2017, **56**, 9966–9972.
- J. Liu, D. Zhu, C. Guo, A. Vasileff and S. Z. Qiao, *Adv. Energy Mater.*, 2017, **7**, 1700518.
- W. Xia, J. Zhu, W. Guo, L. An, D. Xia and R. Zou, *J. Mater. Chem. A*, 2014, **2**, 11606–11613.
- H. x. Zhong, J. Wang, Y. w. Zhang, W. l. Xu, W. Xing, D. Xu, Y. f. Zhang and X. b. Zhang, *Angew. Chem., Int. Ed.*, 2014, **53**, 14235–14239.
- M. J. Song, I. T. Kim, Y. B. Kim, J. Kim and M. W. Shin, *Electrochim. Acta*, 2017, **230**, 73–80.
- A. Banerjee, U. Singh, V. Aravindan, M. Srinivasan and S. Ogale, *Nano Energy*, 2013, **2**, 1158–1163.
- L. Hu, Y. Huang, F. Zhang and Q. Chen, *Nanoscale*, 2013, **5**, 4186–4190.
- L. Zhang, H. B. Wu, S. Madhavi, H. H. Hng and X. W. Lou, *J. Am. Chem. Soc.*, 2012, **134**, 17388–17391.
- S. J. Yang, S. Nam, T. Kim, J. H. Im, H. Jung, J. H. Kang, S. Wi, B. Park and C. R. Park, *J. Am. Chem. Soc.*, 2013, **135**, 7394–7397.
- J. H. Lee, Y. J. Sa, T. K. Kim, H. R. Moon and S. H. Joo, *J. Mater. Chem. A*, 2014, **2**, 10435–10443.
- A. Aijaz, N. Fujiwara and Q. Xu, *J. Am. Chem. Soc.*, 2014, **136**, 6790–6793.
- H. B. Aiyappa, P. Pachfule, R. Banerjee and S. Kurungot, *Cryst. Growth Des.*, 2013, **13**, 4195–4199.
- H.-L. Jiang, B. Liu, Y.-Q. Lan, K. Kuratani, T. Akita, H. Shioyama, F. Zong and Q. Xu, *J. Am. Chem. Soc.*, 2011, **133**, 11854–11857.
- S. J. Yang, T. Kim, J. H. Im, Y. S. Kim, K. Lee, H. Jung and C. R. Park, *Chem. Mater.*, 2012, **24**, 464–470.
- M. Hu, J. Reboul, S. Furukawa, N. L. Torad, Q. Ji, P. Srinivasu, K. Ariga, S. Kitagawa and Y. Yamauchi, *J. Am. Chem. Soc.*, 2012, **134**, 2864–2867.
- G. Wang, L. Zhang and J. Zhang, *Chem. Soc. Rev.*, 2012, **41**, 797–828.
- X. Xu, R. Cao, S. Jeong and J. Cho, *Nano Lett.*, 2012, **12**, 4988–4991.
- W. Xia, R. Zou, L. An, D. Xia and S. Guo, *Energy Environ. Sci.*, 2015, **8**, 568–576.
- W. Bak, H. S. Kim, H. Chun and W. C. Yoo, *Chem. Commun.*, 2015, **51**, 7238–7241.
- S. Bhattacharjee, J.-S. Choi, S.-T. Yang, S. Beom Choi, J. Kim and W.-s. Ahn, *J. Nanosci. Nanotechnol.*, 2010, **10**, 135–141.
- J. Lee, K. Sohn and T. Hyeon, *J. Am. Chem. Soc.*, 2001, **123**, 5146–5147.
- W. C. Yoo, N. Rajabbeigi, E. E. Mallon, M. Tsapatsis and M. A. Snyder, *Microporous Mesoporous Mater.*, 2014, **184**, 72–82.
- B. Liu, H. Shioyama, T. Akita and Q. Xu, *J. Am. Chem. Soc.*, 2008, **130**, 5390–5391.
- N. L. Rosi, J. Kim, M. Eddaoudi, B. Chen, M. O'Keeffe and O. M. Yaghi, *J. Am. Chem. Soc.*, 2005, **127**, 1504–1518.
- A. Ö. Yazaydin, R. Q. Snurr, T.-H. Park, K. Koh, J. Liu, M. D. LeVan, A. I. Benin, P. Jakubczak, M. Lanuza,

- D. B. Galloway, J. J. Low and R. R. Willis, *J. Am. Chem. Soc.*, 2009, **131**, 18198–18199.
- 34 K. Zhang, R. P. Lively, C. Zhang, R. R. Chance, W. J. Koros, D. S. Sholl and S. Nair, *J. Phys. Chem. Lett.*, 2013, **4**, 3618–3622.
- 35 R. Das, P. Pachfule, R. Banerjee and P. Poddar, *Nanoscale*, 2012, **4**, 591–599.
- 36 B. Budiansky and L. Truskinovsky, *J. Mech. Phys. Solids*, 1993, **41**, 1445–1459.
- 37 J. Diao, K. Gall and M. L. Dunn, *Nat. Mater.*, 2003, **2**, 656–660.
- 38 L. Lee, B. Kim, S. Han, H.-E. Kim, M. D. Lee and J. H. Bang, *Small*, 2018, e1801124.
- 39 S. W. Chee, S. F. Tan, Z. Baraissov, M. Bosman and U. Mirsaidov, *Nat. Commun.*, 2017, **8**, 1224–1232.
- 40 B. Y. Guan, L. Yu and X. W. Lou, *Energy Environ. Sci.*, 2016, **9**, 3092–3096.
- 41 A. C. Ferrari, J. C. Meyer, V. Scardaci, C. Casiraghi, M. Lazzeri, F. Mauri, S. Piscanec, D. Jiang, K. S. Novoselov, S. Roth and A. K. Geim, *Phys. Rev. Lett.*, 2006, **97**, 187401.
- 42 J. P. Murray, A. Steinfeld and E. A. Fletcher, *Energy*, 1995, **20**, 695–704.
- 43 Z. Liu, W. Shen, W. Bu, H. Chen, Z. Hua, L. Zhang, L. Li, J. Shi and S. Tan, *Microporous Mesoporous Mater.*, 2005, **82**, 137–145.
- 44 J.-C. Lee, D.-J. Min and S.-S. Kim, *Metall. Mater. Trans. B*, 1997, **28**, 1019–1028.
- 45 R. Wu, X. Qian, F. Yu, H. Liu, K. Zhou, J. Wei and Y. Huang, *J. Mater. Chem. A*, 2013, **1**, 11126–11129.
- 46 L. Wang, H. Gong, C. Wang, D. Wang, K. Tang and Y. Qian, *Nanoscale*, 2012, **4**, 6850–6855.
- 47 Z. Wang, F. Su, S. Madhavi and X. W. Lou, *Nanoscale*, 2011, **3**, 1618–1623.
- 48 Z. Wang, D. Luan, S. Madhavi, C. Ming Li and X. Wen Lou, *Chem. Commun.*, 2011, **47**, 8061–8063.
- 49 B. Wang, J. S. Chen, H. B. Wu, Z. Wang and X. W. Lou, *J. Am. Chem. Soc.*, 2011, **133**, 17146–17148.
- 50 N. Kang, H. Park Ji, J. Choi, J. Jin, J. Chun, G. Jung Il, J. Jeong, J. G. Park, M. Lee Sang, J. Kim Hae and U. Son Seung, *Angew. Chem., Int. Ed.*, 2012, **51**, 6626–6630.
- 51 Z. Wang, D. Luan, S. Madhavi, Y. Hu and X. W. Lou, *Energy Environ. Sci.*, 2012, **5**, 5252–5256.
- 52 J. I. Feldblyum, M. Liu, D. W. Gidley and A. J. Matzger, *J. Am. Chem. Soc.*, 2011, **133**, 18257–18263.
- 53 H. Furukawa, N. Ko, Y. B. Go, N. Aratani, S. B. Choi, E. Choi, A. Ö. Yazaydin, R. Q. Snurr, M. O’Keeffe, J. Kim and O. M. Yaghi, *Science*, 2010, **329**, 424–430.
- 54 K. S. Park, Z. Ni, A. P. Côté, J. Y. Choi, R. Huang, F. J. Uribe-Romo, H. K. Chae, M. O’Keeffe and O. M. Yaghi, *Proc. Natl. Acad. Sci. U. S. A.*, 2006, **103**, 10186–10191.
- 55 T. Grant Glover, G. W. Peterson, B. J. Schindler, D. Britt and O. Yaghi, *Chem. Eng. Sci.*, 2011, **66**, 163–170.
- 56 D. C. Dietzel Pascal, Y. Morita, R. Blom and H. Fjellvåg, *Angew. Chem., Int. Ed.*, 2005, **44**, 6354–6358.